Chinese Physics Letters

LETTER

Revealing Interfacial Orbital Transport in Nonmagnet/Ferromagnet Bilayers by the Absence of Orbital Hall Magnetoresistance

Cite as: Yumin Yang *et al*. 2026 *Chin. Phys. Lett.* **43** 070706

DOI CSTR

Recommended Articles

Enhanced Spin-Orbit Torque Induced by Interfacial Scattering in Ir/Pt Superlattice
Jiahui Li *et al*.
Chin. Phys. Lett. **42**, 057401 (2025)

Electric-Field Control of Spin and Orbital Hall Effects in a Nodal-Ring Heterostructure Independent of Spin-Orbit Coupling
Zhikuan Wang, Wei Tan, Jianfeng Wang, Zeyu Jiang, and Bing Huang
Chin. Phys. Lett. **43**, 040705 (2026)

Helicity-Controlled Spin Hall Angle in 2D Altermagnets with Rashba Spin-Orbit Coupling
Weiwei Chen, Longhai Zeng, and W. Zhu
Chin. Phys. Lett. **42**, 017201 (2025)

Linear Enhancement of Spin–Orbit Torque and Absence of Bulk Rashba Spin Splitting in Perpendicularly Magnetized $[Pt/Co/W]_n$ Superlattices
Zhihao Yan, Zhengxiao Li, Lujun Zhu, Xin Lin, and Lijun Zhu
Chin. Phys. Lett. **42**, 090701 (2025)

Gate-Tunable Strong Spin–Orbit Torque in 2D Weyl Semiconductor Tellurium-Based Heterostructures
Qiqi Zhang *et al*.
Chin. Phys. Lett. **43**, 040712 (2026)

Charge Excitations at Landau Level Crossings in WSe_2-Encapsulated Bilayer Graphene
Yuxuan Zhu, Zhecheng Li, Yixuan Xu, Yurong Ling, Zijun Lin, Zhimou Chen, Zhao Liu, Hailong Fu, and Xi Lin
Chin. Phys. Lett. **43**, 020714 (2026)

A series journal of Chinese Physical Society distributed by IOP Publishing

iopscience.iop.org/cpl | cpl.iphy.ac.cn

Chinese Physics Letters

Chin. Phys. Lett. **43** 070706 (2026)

LETTER

DOI: 10.1088/0256-307X/43/7/070706
CSTR: 32039.14.0256-307X.43.7.070706

Revealing Interfacial Orbital Transport in Nonmagnet/Ferromagnet Bilayers by the Absence of Orbital Hall Magnetoresistance

Yumin Yang(杨雨民)[1,2], Wenqi Xu(徐文奇)[1], Zhicheng Xie(谢志成)[3], Na Lei(雷娜)[4,5], Jianhua Zhao(赵建华)[5], and Dahai Wei(魏大海)[1,2,*]

[1]State Key Laboratory of Semiconductor Physics and Chip Technologies, Institute of Semiconductors, Chinese Academy of Sciences, Beijing 100083, China
[2]College of Materials Science and Opto-Electronic Technology, University of Chinese Academy of Sciences, Beijing 100049, China
[3]Southwest Institute of Technical Physics, Chengdu 610041, China
[4]Fert Beijing Institute, MIIT Key Laboratory of Spintronics, School of Integrated Circuit Science and Engineering, Beihang University, Beijing 100191, China
[5]National Key Laboratory of Spintronics, Hangzhou International Innovation Institute, Beihang University, Hangzhou 311115, China

*Corresponding author. Email: dhwei@semi.ac.cn

Orbital angular momentum transport has emerged as a promising route for spin-orbitronic devices, yet its transport behavior remains under debate and is often assumed to follow the phenomenology of spin transport. Here, we reveal the distinct nature of interfacial orbital transport through the absence of orbital Hall magnetoresistance (OMR) in nonmagnet/ferromagnet bilayers, challenging the general assumption that orbital transport mimics spin transport. Despite the observation of giant orbital torques, which confirms the injection of orbital currents, thickness-dependent magnetoresistance measurements reveal that the magnetoresistance signal is dominated by the intrinsic magnetoresistance of the ferromagnet and current shunting, with no discernible OMR contribution. We attribute this contradiction to magnetization-independent orbital absorption within the ferromagnet, which allows the generation of orbital torque as one relaxation pathway but suppresses the interfacial reflection required for OMR. Additionally, we find that texture-induced magnetoresistance, self-torque, and interfacial effects in Ni-based bilayers may obscure genuine orbital signals, suggesting that caution is required when employing Ni in orbitronic studies. These findings clarify the distinct physical rules governing orbital transport and provide a simple method to distinguish between spin and orbital currents.

Introduction

Over the past decade, spin-related phenomena in systems with strong spin–orbit coupling (SOC), particularly the spin Hall effect (SHE) [1−3] and spin–orbit torque (SOT) [4,5] [Fig. 1(a)], have attracted considerable attention. Recently, research on nonequilibrium orbital angular momentum (OAM) transport, namely orbital current, has expanded the scope of spintronics by harnessing the orbital degree of freedom [6,7]. Distinct from spin, OAM exhibits stronger lattice coupling [8−10] but weaker exchange interaction with the magnetic moment [11,12], offering a distinct channel for angular momentum flow. Moreover, efficient magnetic manipulation via the orbital Hall effect (OHE) [13−16] and orbital torque [17−19] [Fig. 1(c)] has been demonstrated even in light elements with weak SOC, greatly expanding the material landscape of spin-orbitronics beyond heavy metals. However, many interpretations of orbital-related phenomena implicitly assume that orbital transport simply follows the same phenomenological rules as spin transport, that is, the "orbital version" of spin-related effects [6]. Given the fundamentally different nature of OAM [9,15], this spin–orbital analogy might hinder the rational design of efficient spin-orbitronic devices and lead to the misidentification of spin-related signatures in light metals as orbital effects.

A typical distinction between spin and orbital transport lies in their propagation characteristics. Orbital currents exhibit significantly longer transport ranges within ferromagnets (FMs) [20−23], potentially enabling non-local control of magnetization. Beyond bulk transport, interfacial transport at the nonmagnet (NM)/FM interface may reveal deeper discrepancies. In traditional NM/FM bilayers with strong SOC, a typical phenomenon is spin Hall magnetoresistance (SMR) [24−26] [Fig. 1(b)]. Similarly, orbital Hall magnetoresistance (OMR), the orbital counterpart to SMR, has been proposed to interpret the magnetoresistance (MR) in NM/FM bilayers with weak SOC [27,28]. However, current interpretations of these phenomena remain controversial [29,30]. Moreover, orbital transport parameters inferred from OMR [27] differ significantly from those established via orbital torque [20]. These results indicate that orbital transport at the NM/FM interface cannot be simply likened to spin transport.

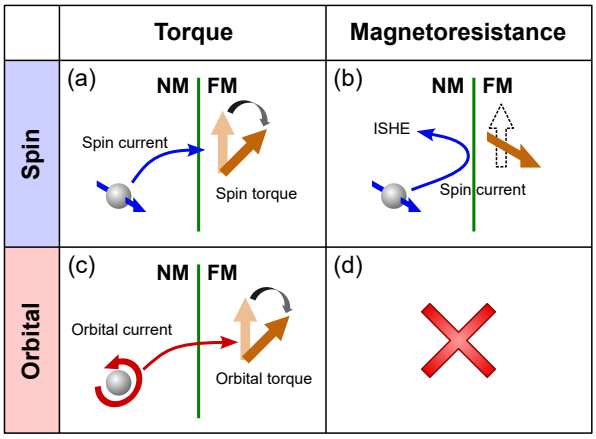

Fig. 1. SOT and magnetoresistance phenomena induced by spin and orbital transport. Schematic illustrations of (a) spin and (c) orbital torque: the spin current induces spin torque at the NM/FM interface, and the orbital current induces orbital torque in the bulk of the FM. (b) Schematic illustration of SMR: when the spin polarization $\boldsymbol{\sigma}_{\text{spin}} \parallel \boldsymbol{M}$, spin currents are reflected, generating SMR. (d) The absence of OMR.

Conventionally, for SMR, the spin current generated by the NM

Received 6 May 2026; accepted 17 June 2026; published 22 July 2026
© 2026 Chinese Physical Society and IOP Publishing Ltd. All rights, including for text and data mining, AI training, and similar technologies, are reserved.

Check for updates

undergoes reflection at the NM/FM interface, and this reflection depends on the relative orientation of the spin polarization $\boldsymbol{\sigma}_{\text{spin}}$ and the magnetization $\boldsymbol{M}$. The difference in spin reflection between $\boldsymbol{\sigma}_{\text{spin}} \parallel \boldsymbol{M}$ and $\boldsymbol{\sigma}_{\text{spin}} \perp \boldsymbol{M}$ subsequently generates various charge currents via the inverse spin Hall effect (ISHE), thereby inducing anisotropic resistance [24,25] [see Fig. 1(b)]. A simple analogy suggests that strong OHE or orbital torque in NM/FM bilayers should naturally be accompanied by a sizable OMR. However, considering that the orbital current couples weakly to the magnetic moment [11,12] and has a longer transport range in the FM [20–23], we propose an alternative physical picture. After entering the FM, the orbital current undergoes $\boldsymbol{M}$-independent absorption within the FM bulk. When the orbital polarization $\boldsymbol{\sigma}_{\text{orb}} \perp \boldsymbol{M}$, part of the absorbed OAM is transferred to the magnetic moment and generates orbital torque, as shown in Fig. 1(c). By contrast, when $\boldsymbol{\sigma}_{\text{orb}} \parallel \boldsymbol{M}$, the absorbed OAM mainly relaxes through other channels, such as lattice or phonon excitations, instead of being strongly reflected at the NM/FM interface. If the OAM undergoes isotropic bulk absorption rather than interface reflection, the anisotropic reflection required for OMR would vanish. Consequently, the OMR, involving multiple transport processes, provides an ideal testbed for characterizing interfacial orbital transport.

In this work, through a systematic study of NM/FM bilayers, we demonstrate that magnetization-independent bulk absorption of the orbital current, together with suppressed interfacial reflection, leads to the absence of OMR. In which Ru and Ti with weak SOC are used as orbital-current sources, while Ni, Co, and Py are used as FMs. Considering the complexity and multiplicity of MR mechanisms, we investigate the dependence of the MR ratio on the NM thickness t_{NM} and carefully control the FM thickness t_{FM} and the NM/FM interface. However, after rigorously excluding the intrinsic mechanisms of the FM and the shunting effects of the NM, the OMR signal is vanishingly small across all samples. Crucially, the observation of giant orbital torques confirms the existence of orbital current in the same devices. This supports our hypothesis that orbital transport is dominated by isotropic bulk absorption in the FM, in contrast to the anisotropic interfacial reflection mechanism of spin transport. Moreover, we point out the complexities and shortcomings of Ni-based heterojunctions in the study of orbital-related effects. Our findings not only clarify the distinction between orbital and spin, but also provide a simple method to distinguish them.

Results and Discussion

Magnetoresistance and Orbital Torque of Ru/Co Bilayers

In order to evaluate the OMR, angular-dependent magnetoresistance (ADMR) measurements were systematically performed on the samples. As illustrated in Fig. 2(a), a charge current was applied along the x-axis of the devices, while an external magnetic field $\boldsymbol{H}$ was rotated within the yz-plane. The normalized ADMR $[R(\beta)-R_0]/R_0$ for the Ru(t)/Co(5) series is shown in Fig. 2(b), and can be described by $R(\beta) = R_0 + \Delta R\cos^2\beta$, similar to that observed in SMR. However, the appearance of this angular dependence alone does not constitute evidence for OMR. It can arise from interfacial SOC [29,31,32], geometric-size effects, and film texture [33–35], all of which are sensitive to t_{FM}. Thus, one possible approach to proving the existence of OMR is to examine the t_{NM}-dependence of the MR ratio $\Delta R/R_0$. Figure 2(c) presents $\Delta R/R_0$ for the Ru(t)/Co(5) series, which monotonically decreases from 8×10^{-4} to 5×10^{-5} as t_{Ru} increases, where $\Delta R = R_\perp - R_\parallel$, and $R_\perp$ and $R_\parallel$ represent the $R(\beta)$ measured with the magnetic field perpendicular ($\beta = 0^\circ$) and parallel ($\beta = 90^\circ$) to the film, respectively. However, the monotonic decay of $\Delta R/R_0$ is likely dominated by the MR mechanisms within the FM layer [35] together with the shunting effect of the NM layer, rather than exhibiting OMR behavior with an asymmetric single peak [which increases rapidly with t_{NM} and then gradually decreases, as in the predicted OMR plotted in Fig. 2(c), to be discussed later]. According to the shunting model, the variation of $\Delta R/R_0$ with t_{NM} caused by current shunting can be approximated to first order as

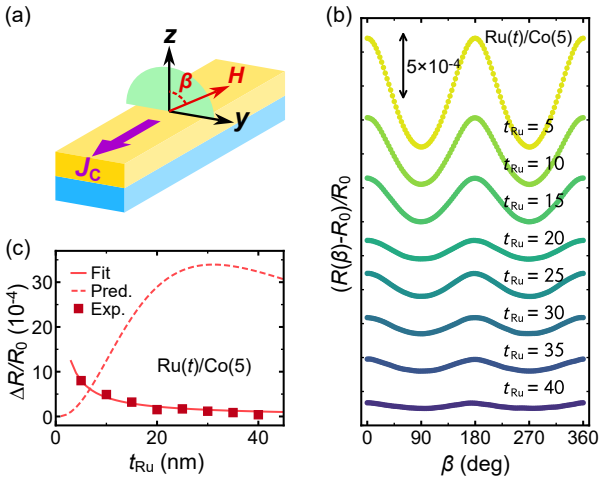

Fig. 2. ADMR measurement of Ru/Co samples. (a) Schematic of the ADMR measurement with the external magnetic field $\boldsymbol{H}$ rotating in the yz-plane (β angle). (b) Normalized angular-dependent resistance $[R(\beta)-R_0)/R_0$ for Ru(t)/Co(5) bilayers. (c) MR ratio $\Delta R/R_0$ as a function of Ru thickness t_{Ru}. The solid line represents the fit to the shunting model, while the dashed line indicates the predicted OMR.

$$\frac{\Delta R}{R_0} = r_0 \Big/ \left(1 + \frac{t_{\text{NM}}\rho_{\text{FM}}}{t_{\text{FM}}\rho_{\text{NM}}}\right), \tag{1}$$

where ρ_{NM} and ρ_{FM} are the resistivities of NM and FM, and r_0 is the MR ratio at $t_{\text{NM}} = 0$. Here, only r_0 was treated as a free parameter, and the resistivities were obtained from R_0, yielding $\rho_{\text{Ru}} = 22.4\,\mu\Omega\cdot\text{cm}$ and $\rho_{\text{Co}} = 167.3\,\mu\Omega\cdot\text{cm}$. Moreover, ρ_{Ru} remains approximately consistent across different thicknesses in the experiment, satisfying the premise of the shunting model [more details are shown in Supplementary Materials (SM) S1]. As shown in Fig. 2(c), the shunting model reproduces well the experimental dependence of $\Delta R/R_0$ on t_{Ru} and significantly differs from the predicted OMR. This result indicates that the ADMR is dominated by the mechanisms of the FM single layer rather than by OMR.

The absence of the OMR might also be attributed to the weak orbital current in the NM/FM bilayer. To rule out this possibility, we conducted spin–torque ferromagnetic resonance (ST-FMR) experiments to measure the orbital torque, thereby verifying the presence of a sizable orbital current. A modulated radio-frequency (RF) current is applied to the ST-FMR devices; a swept in-plane magnetic field $\boldsymbol{H}$ is applied at various azimuthal angles φ to probe the angular dependence of the signal; and the rectified voltage signal V_{DC} is detected using a lock-in amplifier, as illustrated in Fig. 3(a). To avoid the influence of t_{FM} on the orbital absorption and self-torque, we fix t_{FM} and directly measure the SOT effective field instead of the $V_{\text{S}}/V_{\text{A}}$ ratio, where V_{S} and V_{A} are the symmetric and antisymmetric components, respectively. The signal V_{DC} induced by y-polarized OAM and an Oersted field along the y-axis can be expressed as [36,37]

$$\begin{aligned} V_{\text{DC}} &= \frac{I_{\text{RF}}\Delta R_{\text{IP}}\sin 2\varphi\cos\varphi}{2\alpha(2H_{\text{res}}+M_{\text{eff}})}\left(S(H)H_{\text{DL}} + \sqrt{1+\frac{M_{\text{eff}}}{H_{\text{res}}}}A(H)H_{\text{FL+Oe}}\right), \\ S(H) &= \frac{\Delta_H^2}{(H-H_{\text{res}})^2+\Delta_H^2}, \\ A(H) &= \frac{\Delta_H(H-H_{\text{res}})}{(H-H_{\text{res}})^2+\Delta_H^2}, \end{aligned} \tag{2}$$

where the symmetric Lorentzian $S(H)$ associated with damping-like torque H_{DL} contributes to V_{S}, whereas the antisymmetric Lorentzian $A(H)$ associated with $H_{\text{FL+Oe}}$ (the sum of field-like torque H_{FL} and Oersted field H_{Oe}) gives rise to V_{A}. H_{res} is the resonance field, and Δ_H is the half-width-at-half-maximum linewidth. M_{eff} is the effective magnetization fitted by the Kittel formula $2\pi f = \gamma\sqrt{H_{\text{res}}(H_{\text{res}}+M_{\text{eff}})}$, and γ is the gyromagnetic ratio. α is the Gilbert damping coefficient

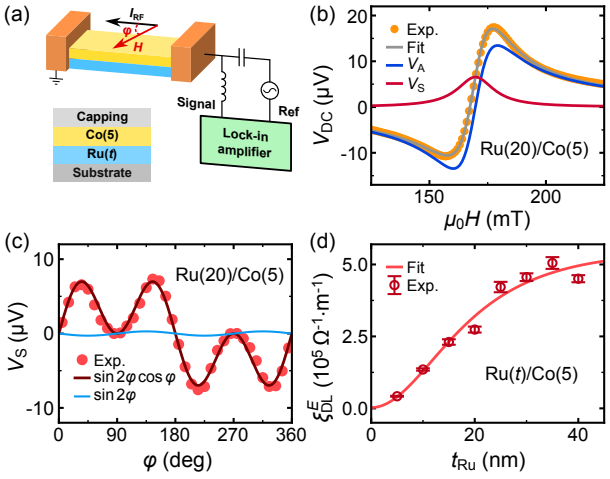

Fig. 3. ST-FMR measurement of Ru/Co samples. (a) Schematic of the ST-FMR measurement setup. (b) Magnetic field dependence of the rectified voltage V_{DC} for Ru(20)/Co(5), decomposed into symmetric (V_S) and antisymmetric (V_A) Lorentzian components. (c) Angular dependence of V_S fitted by a function with $\sin 2\varphi\cos\varphi$ and $\sin 2\varphi$ contributions. (d) Damping-like torque efficiency ξ^E_{DL} as a function of Ru thickness t_{Ru} for the Ru(t)/Co(5) series, fitted by the drift-diffusion model.

fitted by $\Delta_H = 2\pi f\alpha/\gamma + W_0$. ΔR_{IP} is the amplitude of the in-plane ADMR arising from anisotropic magnetoresistance and other mechanisms, obtained from $R(\varphi) = R_0 + \Delta R_{IP}\cos^2\varphi$. I_{RF} is the amplitude of the RF current measured by comparing the resistance changes induced by the Joule heating of RF and DC currents. More details are shown in SM S2. Figure 3(b) shows the typical H dependence of V_{DC}, the fitted $S(H)$ contribution V_S and $A(H)$ contribution V_A of the sample Ru(20)/Co(5) at $f = 14$ GHz and $\varphi = 35°$. The significant V_S signal indicates the existence of H_{DL}. To exclude the influence of the antisymmetric current on the signal, the φ dependence of V_S is extracted [see Fig. 3(c)]. The fitting curve is mainly dominated by the $\sin 2\varphi\cos\varphi$ component, whereas the $\sin 2\varphi$ component caused by the z-component of Oersted field is much smaller. Considering the weak SHE of Ru [38], H_{DL} can be regarded as a signature of orbital torque. In addition, the H_{FL+Oe} of Ru(t)/Co(5) is dominated by the H_{Oe} contribution, with no discernible H_{FL} induced by OAM, as discussed in SM S3. To normalize the orbital torque, we calculated SOT efficiency by

$$\xi^E_{DL} = \frac{2e}{\hbar}\frac{\mu_0 M_S t_{FM} H_{DL}}{E}, \tag{3}$$

where E is the electric field obtained from $I_{RF}R_0/l$ (l is the device length), and M_S is the saturation magnetization.

To obtain the orbital transport information of Ru, the t_{Ru}-dependent SOT is evaluated. Figure 3(d) shows ξ^E_{DL} for Ru(t)/Co(5) with various t_{Ru}, and a significant orbital torque is observed. ξ^E_{DL} increases from $0.5\times10^5\,\Omega^{-1}\cdot\mathrm{m}^{-1}$ to about $5\times10^5\,\Omega^{-1}\cdot\mathrm{m}^{-1}$ and gradually saturates. We describe this behavior using the drift-diffusion model,

$$\xi^E_{DL} = \eta_{stack}\sigma^{eff}_{OH}\left(1 - \mathrm{sech}\frac{t_{NM}}{\lambda_{NM}}\right) + \xi^E_{DL,0}, \tag{4}$$

where λ_{NM} is the diffusion length of the orbital current in the NM, σ^{eff}_{OH} is the effective orbital Hall conductivity, and $\xi^E_{DL,0}$ is the contribution from self-torque or interfacial effects. Here, η_{stack} is a stacking-order factor, with $\eta_{stack} = 1$ for NM/FM and $\eta_{stack} = -1$ for FM/NM. As shown in Fig. 3(d), the drift-diffusion model fits various ξ^E_{DL} well, yielding $\lambda_{Ru} = 13.1 \pm 2.4$ nm, $\sigma^{eff}_{OH} = 5.45\times10^5\,\Omega^{-1}\cdot\mathrm{m}^{-1}$, and a negligible $\xi^E_{DL,0}$ for Ru(t)/Co(5). The σ^{eff}_{OH} of Ru/Co is significantly higher than that of Pt/Co [39] (about $2\times10^5\,\Omega^{-1}\cdot\mathrm{m}^{-1}$). Moreover, λ_{Ru} indicates long-range diffusion transport of the orbital current in Ru, similar to that in Ti and W [20]. Since the diffusion length exceeds the electron mean free path in Ru and no significant resistivity gradient is observed in the sample (see SM S1), the orbital current induced by current density gradient [40] at interfaces can be ruled out. Importantly, the strong orbital torque indicates the existence of a large orbital current generated by Ru.

Absence of Orbital Hall Magnetoresistance

The contradiction between the strong orbital torque and the vanishing OMR demonstrates the breakdown of the spin–orbital analogy for OMR. To analyze these phenomena, we construct an OMR model referencing the SMR model [25], which can be expressed by

$$\begin{aligned}\frac{\Delta R}{R_0} &= \theta^2_{OH}\frac{\lambda_{NM}}{t_{NM}}\frac{\tanh^2(t_{NM}/2\lambda_{NM})}{1 + t_{FM}\rho_{NM}/t_{NM}\rho_{FM}} \\ &\quad\cdot\left[\frac{g_R}{1 + g_R\coth(t_{NM}/\lambda_{NM})} - \frac{g_F}{1 + g_F\coth(t_{NM}/\lambda_{NM})}\right], \\ g_R &\equiv 2\rho_{NM}\lambda_{NM}\mathrm{Re}\left[G^{orb}_{mix}\right], \\ g_F &\equiv \eta\rho_{NM}\lambda_{NM}/\rho_{FM}\lambda_{FM}\coth(t_{FM}/\lambda_{FM}),\end{aligned} \tag{5}$$

where the orbital Hall angle θ_{OH} and λ_{NM} can be obtained from orbital torque measurement; g_R and g_F are the normalized interfacial orbital conductance for $\boldsymbol{\sigma}_{orb} \perp \boldsymbol{M}$ and $\boldsymbol{\sigma}_{orb} \parallel \boldsymbol{M}$, respectively. G^{orb}_{mix} denotes the interfacial orbital mixing conductance, and η is the orbital absorption efficiency when $\boldsymbol{\sigma}_{orb} \parallel \boldsymbol{M}$. In an ideal situation, $g_R \gg 1$ and $g_F = 0$. The first and second terms in the square brackets of Eq. (5), involving g_R and g_F, denote the absorption of the orbital current when $\boldsymbol{\sigma}_{orb} \perp \boldsymbol{M}$ and $\boldsymbol{\sigma}_{orb} \parallel \boldsymbol{M}$, respectively. Here, we initially assume an ideal Ru/Co interface with an interfacial orbital transparency $T_{orb} \approx 1$. Thus, θ_{OH} can be approximated by the effective orbital Hall angle $\theta^{eff}_{OH} = \rho_{NM}\sigma^{eff}_{OH} = T_{orb}\theta_{OH}$. Then, we assume $g_R = 10$ and $g_F = 0.1$ by analogy with SMR [25]. The $\Delta R/R_0$ predicted by this model is plotted in Fig. 2(c). Clearly, the predicted OMR significantly deviates from the experimental data. This discrepancy indicates that if orbital transport followed the same phenomenology as spin transport, a detectable OMR signal should emerge. The absence of observable OMR therefore points to a fundamental difference between spin and orbital transport.

The observed SMR and the absence of OMR arise from the distinct coupling properties and relaxation behaviors of spin and orbital angular momentum. Spin angular momentum (SAM) couples strongly to $\boldsymbol{M}$, so its transport is strongly influenced by $\boldsymbol{M}$. When $\boldsymbol{\sigma}_{spin} \perp \boldsymbol{M}$ the spin current is absorbed by the FM layer and induces SOT [Fig. 4(a)]; whereas when $\boldsymbol{\sigma}_{spin} \parallel \boldsymbol{M}$, the spin current is reflected by the FM and causes magnetoresistance variations via ISHE [24,25] [Fig. 4(b)]. Moreover, in 3d metals with weak SOC, spin–lattice coupling is relatively weak and SAM can be approximately conserved over short length scales. As a result, from the perspective of angular momentum conservation, when $\boldsymbol{\sigma}_{spin} \perp \boldsymbol{M}$ the SAM is transferred to the magnetic moment; whereas when $\boldsymbol{\sigma}_{spin} \parallel \boldsymbol{M}$, strong spin accumulation can develop near the interface and inside the FM, leading to enhanced spin reflection. It should be noted that the previously discussed short propagation length of the spin current in the FM refers mainly to the case relevant to SOT, that is, the case of $\boldsymbol{\sigma}_{spin} \perp \boldsymbol{M}$, where spin dephasing dominates the relaxation process [41]. In contrast, when $\boldsymbol{\sigma}_{spin} \parallel \boldsymbol{M}$, spin relaxation dominated by spin-flip scattering in an FM with weak SOC is slower, allowing the spin transport length to reach several tens of nanometers [42]. In summary, the $\boldsymbol{M}$-dependent spin absorption and reflection are the key to SMR.

In contrast, OAM couples weakly to the magnetic moment [11,12], which suppresses the $\boldsymbol{M}$-dependent OAM reflection at the NM/FM interface that is required to generate OMR via the inverse OHE [Figs. 4(c) and 4(d)]. From the perspective of angular momentum transfer, the absorbed OAM can relax through multiple pathways after entering the FM bulk, with orbital torque representing only one of them. When $\boldsymbol{\sigma}_{orb} \perp \boldsymbol{M}$ part of the absorbed OAM transfers angular momentum to the magnetic moment and generates orbital torque [Fig. 4(c)]. When $\boldsymbol{\sigma}_{orb} \parallel \boldsymbol{M}$, the absorbed OAM predominantly relaxes through other channels, such as phonon excitations [9,10] [Fig. 4(d)]. Owing to the strong coupling between OAM and the lattice [8], OAM can rapidly dissipate into the lattice and is generally nonconserved in

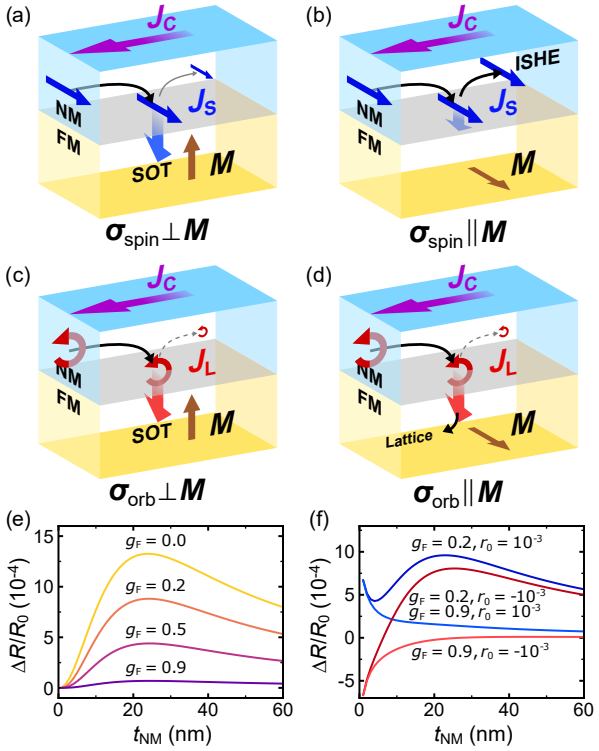

Fig. 4. Reasons for the absence of OMR. (a)–(d) Schematic comparison of spin (top two) and orbital (bottom two) transport at the NM/FM interface, where blue straight arrows and red curved arrows represent spin and orbital angular momentum, respectively. For $\boldsymbol{\sigma} \perp \boldsymbol{M}$, both (a) spin current J_S and (c) orbital current J_L transfer angular momentum to the FM. For $\boldsymbol{\sigma} \parallel \boldsymbol{M}$, (b) the spin current is reflected and generates SMR, whereas (d) the orbital current is mainly absorbed in the FM, suppressing the reflection required for OMR. (e) Calculated OMR as a function of NM-thickness t_{NM} for varying orbital absorption g_F. (f) Simulated total MR ratio combining OMR and intrinsic FM magnetoresistance r_0. A large g_F renders the OMR signal indistinguishable from background contributions from the FM.

solids [40]. Consequently, even when $\boldsymbol{\sigma}_{orb} \parallel \boldsymbol{M}$, the absence of OAM reflection does not lead to more OAM accumulation in the FM layer. In other words, $\boldsymbol{M}$ mainly determines the transfer and relaxation pathways of the injected OAM rather than its interfacial reflection.

Within the OMR framework, the failure to reproduce the experimental results can be traced to the parameter g_F. In conventional SMR, the strong coupling between spin and the magnetic moment, and the weak coupling between spin and the lattice, result in strong interfacial spin reflection and weak spin absorption when $\boldsymbol{\sigma}_{spin} \parallel \boldsymbol{M}$, leading to a small g_F value. In contrast, for orbital transport, the strong orbital absorption by the FM when $\boldsymbol{\sigma}_{orb} \parallel \boldsymbol{M}$ implies that g_F approaches the magnitude of g_R. To illustrate this, figure 4(e) shows the simulated impact of g_F on the OMR, where $\theta_{OH} = 0.1$, $g_R = 1$, $\lambda_{NM} = 10$ nm, $t_{FM} = 5$ nm, $\rho_{NM} = 20\,\mu\Omega\cdot$cm, and $\rho_{FM} = 50\,\mu\Omega\cdot$cm. Clearly, the OMR reduces significantly as g_F increases. Furthermore, considering the contributions of other MR mechanisms from the FM layer and current shunting on $\Delta R/R_0$, the t_{NM}-dependence of the OMR becomes submerged within these contributions and difficult to separate, as shown in Fig. 4(f).

Magnetoresistance and Orbital Torque of Ni-Based Bilayers

To further investigate the orbital torque and OMR in NM/FM bilayers, we also examine Ni-based bilayers commonly used in orbital-related studies, including Ru(t)/Ni(8), Ni(8)/Ru(t), and Ni(8)/Ti(t). In these samples, we consider both the deposition order and the choice of NM, because both Ti and Ru possess strong OHE but negligible SHE [38,43]. Importantly, the ADMR analysis for Ni-based films differs from that used previously, because the ADMR curves significantly deviate from a $\cos^2\beta$ dependence (see SM S4). This behavior originates from the growth-induced texture of Ni, in which crystalline anisotropy causes higher-order contributions in Ni-based films [44]. As a result, compared with the above approach using $\Delta R = R_\perp - R_\parallel$, a fitting function $R = R_0 + \sum_n \Delta R_{2n} \cos^{2n}\beta$ that includes higher-order terms is necessary. Here, n takes values from 1 to 4 for all samples, where the ΔR_2 term represents the underlying OMR, SMR, or other MR mechanisms, whereas high-order terms ΔR_4, ΔR_6, and ΔR_8 are induced by crystalline anisotropy (for more details, see SM S4). To demonstrate the necessity of these higher-order terms, we compare the MR ratios obtained from two methods in the Pt(t)/Ni(8) series. Only the $\Delta R/R_0$ extracted from the high-order fitting, that is, $\Delta R_2/R_0$, follows the expected t_{NM}-dependence of the SMR effect [25] (see SM S5).

Subsequently, the high-order analysis is used for the Ru(t)/Ni(8), Ni(8)/Ru(t), and Ni(8)/Ti(t) series to extract the t_{NM}-dependence $\Delta R/R_0$ as shown in Figs. 5(a)–5(c) (more detailed results shown in SM S6). For Ni(8)/Ru(t) and Ni(8)/Ti(t) with Ni grown at the bottom, the $\Delta R/R_0$ are negative and monotonically decrease from 4×10^{-4} to 5×10^{-5} with increasing t_{NM}, similar to Ru(t)/Co(5) [see Figs. 5(b) and 5(c)]. These behaviors are well reproduced by the shunting model [solid lines in Figs. 5(b) and 5(c)], indicating that no OMR is observed. In contrast, as shown in Fig. 5(a), the $\Delta R/R_0$ for Ru(t)/Ni(8) exhibits a sign reversal from negative to positive at $t_{Ru} = 10$ nm and first increases and then decreases, forming a peak at $t_{Ru} = 15$–20 nm. Although Ru(t)/Ni(8) exhibits peak-like behavior, this peak arises from a sign reversal of $\Delta R/R_0$ induced by the texture of the Ni layer [44] rather than OMR. The lower-order MR term ΔR_2 of the Ni film is sensitive to structural details including the buffer layer, which might complicate the analysis of $\Delta R/R_0$. One piece of evidence is the influence of the buffer layer on $\Delta R/R_0$ in Ru(t)/Ni(8) and Pt(t)/Ni(8), where the samples with and without an amorphous SiO_2 buffer layer show different $\Delta R/R_0$ (see SM S7). For the Ni(8)/Ru(t) samples, since Ni is deposited first, its structural properties remain independent of the thickness of the Ru overlayer, and $\Delta R/R_0$ therefore shows a stable monotonic decrease dominated by current shunting. However, in the Ru(t)/Ni(8) samples, the strong structural sensitivity of Ni means that variations in the underlying Ru layer influence the Ni texture, resulting in a sign reversal of $\Delta R/R_0$. Moreover, the $\Delta R/R_0$ values of Ni(8)/Ti(t), Ni(8)/Ru(t), and Ru(5)/Ni(8) are all negative, which further supports the conclusion that the sign reversal in Ru(t)/Ni(8) originates from structural evolution. In summary, no trace of OMR is observed in these series.

However, significant orbital torques are observed in all three series [see Figs. 5(e)–5(g); more details are shown in SM S8]. For Ru(t)/Ni(8), ξ^E_{DL} increases and gradually saturates with t_{Ru}. For Ni(8)/Ru(t) and Ni(8)/Ti(t), ξ^E_{DL} decreases with increasing t_{Ru} or t_{Ti} due to the reversed deposition order, and Ni(8)/Ti(t) does not exhibit saturation behavior because of the longer λ_{Ti}. Furthermore, all t_{NM}-dependent ξ^E_{DL} are well described by the drift-diffusion model, and the extracted parameters are summarized in Table 1. The fitted λ_{Ru} of Ru(t)/Ni(8) and Ni(8)/Ru(t) are consistent with that obtained in the Ru(t)/Co(5) series. And λ_{Ti}, determined to be 44.1 ± 2.3 nm, is consistent with the previously reported large orbital diffusion length [20]. Moreover, all fitted curves of the Ni-based series deviate from 0 at $t_{NM} = 0$, indicating significant $\xi^E_{DL,0}$, which might arise from larger self-torque or interfacial effects in Ni-based bilayers. Notably, Ru(t)/Ni(8) exhibits a higher SOT efficiency than Ni(8)/Ru(t), which may originate from the difference in interfacial orbital transparency caused by the deposition order, as reported previously [20,45]. In addition, Ru(t)/Co(5) has a higher ξ^E_{DL} compared with Ru(t)/Ni(8), which might originate from a higher orbital transparency at the Ru/Co interface, and strong orbital torques in Co have also been reported previously [46].

Based on the orbital torque measurements, we also predict the corresponding OMR. Because ξ^E_{DL} in Ru(t)/Ni(8) and Ni(8)/Ru(t) is weaker than that in Ru(t)/Co(5), the assumptions of an ideal interface and $g_R \gg 1$ do not hold. Thus, we assume $\theta_{OH} = 0.12$ based on Ru(t)/Co(5), and g_R can be calculated from $\theta^{eff}_{OH} = T_{orb}\theta_{OH}$ and

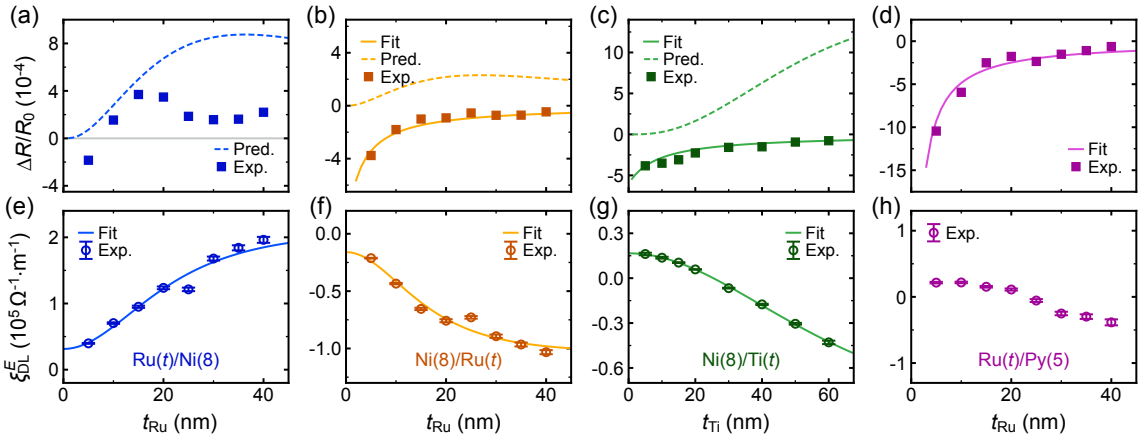

Fig. 5. ADMR and orbital torque of Ni-based samples. The NM-thickness t_{NM}-dependence of MR ratios $\Delta R/R_0$ for (a) Ru(t)/Ni(8), (b) Ni(8)/Ru(t), (c) Ni(8)/Ti(t), and (d) Ru(t)/Py(5) series. The solid line represents the fit to the shunting model, while the dashed line indicates the predicted OMR. (e)–(h) Corresponding orbital torque efficiency ξ^E_{DL} for the respective series, fitted by the drift-diffusion model.

Table 1. The fitted results and parameters for the drift-diffusion model of orbital torque, the shunting model of ADMR and the OMR model.

	λ_{NM} (nm)	σ^{eff}_{OH} ($10^5\,\Omega^{-1}\cdot m^{-1}$)	$\xi^E_{DL,0}$ ($10^5\,\Omega^{-1}\cdot m^{-1}$)	ρ_{NM} ($\mu\Omega\cdot cm$)	ρ_{FM} ($\mu\Omega\cdot cm$)	r_0 (10^{-4})
Ru(t)/Co(5)	13.1 ± 2.4	5.45 ± 0.48	0.03 ± 0.42	22.4	164	66.8 ± 3.3
Ru(t)/Ni(8)	14.8 ± 2.3	1.77 ± 0.22	0.31 ± 0.04	22.4	37.2	–
Ni(8)/Ru(t)	11.3 ± 2.0	0.87 ± 0.08	−0.16 ± 0.08	20.9	64.5	−10.0 ± 0.64
Ni(8)/Ti(t)	44.1 ± 2.3	1.14 ± 0.07	0.17 ± 0.01	71.3	64.5	−6.04 ± 0.25
Ru(t)/Py(5)	–	–	–	22.4	229	−104 ± 5.8

$T_{orb} = g_R/(1+g_R)$ [47]. For Ni(8)/Ti(t), we still assume an ideal interface, use θ^{eff}_{OH} as θ_{OH}, and set $g_R = 10$ as in Ru(t)/Co(5). As shown by the dashed lines in Figs. 5(a)–5(c), the OMR predicted by the model is remarkably large and apparently deviates from experimental data. This further supports our hypothesis that the OMR signal is extremely weak.

To further demonstrate that the SOT comes from orbital torque and the ADMR is independent of the interaction between orbital current and the magnetic moment, we measure the Ru(t)/Py(5) series using Py with weak orbital torque [20,48] as the FM. For the ADMR, $\Delta R/R_0$ obtained from $\Delta R = R_\perp - R_\parallel$ is negative and monotonically decreases from 1×10^{-3} to 5×10^{-5} with increasing t_{NM}, similar to previous results and might arise from geometric-size effects and other intrinsic mechanisms [32,34]. Moreover, the evolution of $\Delta R/R_0$ with t_{Ru} can also be well described by the shunting model, as shown by the solid line in Fig. 5(d). As shown in Fig. 5(h), ξ^E_{DL} for Ru(t)/Py(5) is small, which indicates that orbital torque dominates SOT in the previous experiment. These results indicate that the appearance and variation of the ADMR are not correlated with the orbital torque. Instead, the ADMR mainly arises from interface-related effects, geometric-size effects, and other mechanisms inherent to the FM layer.

Based on the above results and discussion, we emphasize that Ni-based bilayers are not ideal candidates for investigating orbital- or even spin-related effects. For instance, we observe that the texture of Ni films introduces ADMR contributions and generates artifacts driven by texture evolution, which are sensitive to the buffer-layer thickness and structure. Furthermore, in SOT measurements, Ni-based bilayers exhibit significant self-torques or interfacial effects. The results in Table 1 show that the Ni-based bilayers exhibit much larger $\xi^E_{DL,0}$ than the Co-based bilayer, and that the magnitude of $\xi^E_{DL,0}$ relative to σ^{eff}_{OH} is also larger in the Ni-based systems. These contributions can reduce or enhance the orbital torque [49], which may interfere with the evaluation of OHE, particularly in experiments that lack t_{NM}-dependence or use t_{NM} below λ_{NM}. A typical controversy highlights this issue: whether the positive SOT observed in Ta/Ni originates from the orbital torque [19,50] or self-torque [51].

Conclusion

In conclusion, our measurements reveal a contrast between giant orbital torques and the absence of observable OMR in Ru/FM and Ti/FM bilayers. The variation in ADMR is entirely dominated by MR mechanisms in the FM layer combined with current shunting, with a negligible contribution from orbital transport. We attribute this to the distinct relaxation mechanisms of orbital currents compared with spin currents: orbital currents are absorbed in the FM bulk regardless of whether the orbital polarization is parallel or perpendicular to the magnetization. The absorbed OAM can relax either by transferring angular momentum to the magnetic moment, thereby producing orbital torque, or through lattice-related channels. This isotropic bulk absorption suppresses the reflection anisotropy essential for OMR. Our findings challenge the direct spin–orbital analogy for orbital phenomena and suggest the need to re-examine the mechanisms of orbital-related effects.

Experimental Section

Sample Preparation

All NM/FM bilayers were prepared by magnetron sputtering at room temperature under a base pressure of 10^{-9} Torr. The heterojunction films were deposited on sapphire substrates with SiO_2(10)/Ti(2) buffer layers and capped by Ti(1)/SiO_2(10), where the numbers in parentheses represent the thicknesses in nanometers and the layer sequence corresponds to the deposition order. For the buffer layers, an amorphous SiO_2(10) layer was introduced to provide an isotropic surface similar to that of thermally oxidized silicon substrates, thereby avoiding the in-plane anisotropy that can be induced in metallic layers by crystalline sapphire substrates. The ultrathin Ti layers in both the buffer and capping structures were used to improve the adhesion between the metal layers and SiO_2. Because the ultrathin Ti layers directly contacting SiO_2 possess high resistivity, their influence on the electrical transport measurements is negligible. In addition, the

Ru(t)/Ni(8) and Pt(t)/Ni(8) samples for the buffer-layer control in SM S7 used only Ti(2) as the buffer layer. To minimize sample-to-sample variations, movable shutters were employed during deposition, so that four samples with different t_{NM} could be fabricated within a single growth process. After deposition, the films were patterned into devices using standard photolithography and ion-beam etching. Metallic electrodes were subsequently fabricated by magnetron sputtering and a lift-off process.

Magnetic Properties and Transport Measurements

The M_S of the FMs was measured using the vibrating sample magnetometer option of a Physical Property Measurement System (PPMS, Quantum Design). ADMR measurements were carried out in the PPMS at 300 K. To minimize the angular deviation between magnetization direction $\boldsymbol{M}$ and $\boldsymbol{H}$, magnetic fields of 5 T and 9 T were applied for Ni-based (including Py) and Co-based samples, respectively. Electrical resistance was measured using a four-probe configuration with a current source (Keithley 6221) and a nanovoltmeter (Keithley 2182A). ST-FMR measurements were performed at room temperature using an electromagnet-based measurement system. Microwave signals at different frequencies with a power of 100 mW were applied using an RF signal generator. The rectified voltage signal was detected with a lock-in amplifier (SR830).

Acknowledgements

This work was supported by the Chinese Academy of Sciences project for Yong Scientists in Basic Research (Grant No. YSBR-030) and the National Natural Science Foundation of China (Grant No. 12474102).

References

[1] Hirsch J E 1999 *Phys. Rev. Lett.* **83** 1834
[2] Hoffmann A 2013 *IEEE Transactions on Magnetics* **49** 5172
[3] Sinova J, Valenzuela S O, Wunderlich J, Back C H, and Jungwirth T 2015 *Rev. Mod. Phys.* **87** 1213
[4] Manchon A, Železný J, Miron I M, Jungwirth T, Sinova J, Thiaville A, Garello K, and Gambardella P 2019 *Rev. Mod. Phys.* **91** 035004
[5] Shao Q, Li P, Liu L, Yang H, Fukami S, Razavi A, Wu H, Wang K, Freimuth F, Mokrousov Y, Stiles M D, Emori S, Hoffmann A, Akerman J, Roy K, Wang J P, Yang S H, Garello K, and Zhang W 2021 *IEEE Trans. Magn.* **57** 1
[6] Fukami S, Lee K J, and Kläui M 2025 *Nat. Phys.*
[7] Kim J and Otani Y 2022 *Journal of Magnetism and Magnetic Materials* **563** 169974
[8] Urazhdin S 2023 *Phys. Rev. B* **108** L180404
[9] Han S, Lee H W, and Kim K W 2022 *Phys. Rev. Lett.* **128** 176601
[10] Han S, Ko H W, Oh J H, Lee H W, Lee K J, and Kim K W 2025 *Phys. Rev. Lett.* **134** 036305
[11] Lee S, Kang M G, Go D, Kim D, Kang J H, Lee T, Lee G H, Kang J, Lee N J, Mokrousov Y, Kim S, Kim K J, Lee K J, and Park B G 2021 *Commun. Phys.* **4** 234
[12] Sala G and Gambardella P 2022 *Phys. Rev. Research* **4** 033037
[13] Tanaka T, Kontani H, Naito M, Naito T, Hirashima D S, Yamada K, and Inoue J 2008 *Phys. Rev. B* **77** 165117
[14] Kontani H, Tanaka T, Hirashima D S, Yamada K, and Inoue J 2009 *Phys. Rev. Lett.* **102** 016601
[15] Go D, Jo D, Kim C, and Lee H W 2018 *Phys. Rev. Lett.* **121** 086602
[16] Jo D, Go D, and Lee H W 2018 *Phys. Rev. B* **98** 214405
[17] Go D and Lee H W 2020 *Phys. Rev. Research* **2** 013177
[18] Go D, Freimuth F, Hanke J P, Xue F, Gomonay O, Lee K J, Blügel S, Haney P M, Lee H W, and Mokrousov Y 2020 *Phys. Rev. Research* **2** 033401
[19] Lee D, Go D, Park H J, Jeong W, Ko H W, Yun D, Jo D, Lee S, Go G, Oh J H, Kim K J, Park B G, Min B C, Koo H C, Lee H W, Lee O, and Lee K J 2021 *Nat. Commun.* **12** 6710
[20] Hayashi H, Jo D, Go D, Gao T, Haku S, Mokrousov Y, Lee H W, and Ando K 2023 *Commun. Phys.* **6** 32
[21] Yang Y, Xie Z, Zhao Z, Lei N, Zhao J, and Wei D 2024 *Commun. Phys.* **7** 336
[22] Bose A, Kammerbauer F, Gupta R, Go D, Mokrousov Y, Jakob G, and Kläui M 2023 *Phys. Rev. B* **107** 134423
[23] Ding S, Noël P, Krishnaswamy G K, and Gambardella P 2022 *Phys. Rev. Research* **4** L032041
[24] Chen Y T, Takahashi S, Nakayama H, Althammer M, Goennenwein S T B, Saitoh E, and Bauer G E W 2013 *Phys. Rev. B* **87** 144411
[25] Kim J, Sheng P, Takahashi S, Mitani S, and Hayashi M 2016 *Phys. Rev. Lett.* **116** 097201
[26] Kawaguchi M, Towa D, Lau Y C, Takahashi S, and Hayashi M 2018 *Appl. Phys. Lett.* **112** 202405
[27] Hayashi H and Ando K 2023 *Appl. Phys. Lett.* **123** 172401
[28] Ding S, Liang Z, Go D, Yun C, Xue M, Liu Z, Becker S, Yang W, Du H, Wang C, Yang Y, Jakob G, Kläui M, Mokrousov Y, and Yang J 2022 *Phys. Rev. Lett.* **128** 067201
[29] Chou L H, Mai S C, Li W Y, Lee M H, Chuang C, and Qu D 2023 *Phys. Rev. B* **108** 184422
[30] Zhu Z, Cheng L, Li C, Dou C, Li M, Meng K, Wu Y, Chen J, Xu X, and Jiang Y 2023 *IEEE Transactions on Magnetics* **59** 1
[31] Nakayama H, Kanno Y, An H, Tashiro T, Haku S, Nomura A, and Ando K 2016 *Phys. Rev. Lett.* **117** 116602
[32] Kang M G, Go G, Kim K W, Choi J G, Park B G, and Lee K J 2020 *Nat. Commun.* **11** 3619
[33] Chen T T and Marsocci V A 1972 *J. Appl. Phys.* **43** 1554
[34] Rijks Th G S M, Lenczowski S K J, Coehoorn R, and de Jonge W J M 1997 *Phys. Rev. B* **56** 362
[35] Gil W, Görlitz D, Horisberger M, and Kötzler J 2005 *Phys. Rev. B* **72** 134401
[36] Karimeddiny S, Mittelstaedt J A, Buhrman R A, and Ralph D C 2020 *Phys. Rev. Appl.* **14** 024024
[37] Nan T, Quintela C X, Irwin J, Gurung G, Shao D F, Gibbons J, Campbell N, Song K, Choi S Y, Guo L, Johnson R D, Manuel P, Chopdekar R V, Hallsteinsen I, Tybell T, Ryan P J, Kim J W, Choi Y, Radaelli P G, Ralph D C, Tsymbal E Y, Rzchowski M S, and Eom C B 2020 *Nat. Commun.* **11** 4671
[38] Behera N, Singh M S, Chaudhary S, Pandya D K, and Muduli P K 2015 *J. Appl. Phys.* **117** 17A
[39] Nguyen M H, Ralph D C, and Buhrman R A 2016 *Phys. Rev. Lett.* **116** 126601
[40] Valet T, Jaffrès H, Cros V, and Raimondi R 2025 *Phys. Rev. Lett.* **135** 256301
[41] Ghosh A, Auffret S, Ebels U, and Bailey W E 2012 *Phys. Rev. Lett.* **109** 127202
[42] Bass J and Pratt W P 2007 *J. Phys.: Condens. Matter* **19** 183201
[43] Du C, Wang H, Yang F, and Hammel P C 2014 *Phys. Rev. B* **90** 140407
[44] Philippi-Kobs A, Farhadi A, Matheis L, Lott D, Chuvilin A, and Oepen H P 2019 *Phys. Rev. Lett.* **123** 137201
[45] Fukunaga R, Haku S, Gao T, Hayashi H, and Ando K 2024 *Phys. Rev. B* **109** 144412
[46] Liu F, Liang B, Xu J, Jia C, and Jiang C 2023 *Phys. Rev. B* **107** 054404
[47] Pai C F, Ou Y, Vilela-Leão L H, Ralph D C, and Buhrman R A 2015 *Phys. Rev. B* **92** 064426
[48] Fukunaga R, Haku S, Hayashi H, and Ando K 2023 *Phys. Rev. Res.* **5** 023054
[49] Song Y 2025 *Phys. Rev. Appl.* **24** 024068
[50] Zhang Z, Zhang J, Weng Z, Li J, Song H, and Lin W 2025 *Phys. Rev. B* **111** 104412
[51] Liu Q and Zhu L 2025 *Nat. Commun.* **16** 8660